Implementation of a Locally Conservative Numerical Subgrid Upscaling Scheme for Two-Phase Darcy Flow

Todd Arbogast

Department of Mathematics; C1200, The University of Texas at Austin, Austin,
TX 78712, USA, arbogast@math.utexas.edu

Abstract. We present a locally mass conservative scheme for the approximation of two-phase flow in a porous medium that allows us to obtain detailed fine scale solutions on relatively coarse meshes. The permeability is assumed to be resolvable on a fine numerical grid, but limits on computational power require that computations be performed on a coarse grid. We define a two-scale mixed finite element space and resulting method, and describe in detail the solution algorithm. It involves a coarse scale operator coupled to a subgrid scale operator localized in space to each coarse grid element. An influence function (numerical Greens function) technique allows us to solve these subgrid scale problems independently of the coarse grid approximation. The coarse grid problem is modified to take into account the subgrid scale solution and solved as a large linear system of equations posed over a coarse grid. Finally, the coarse scale solution is corrected on the subgrid scale, providing a fine grid representation of the solution. Numerical examples are presented, which show that near-well behavior and even extremely heterogeneous permeability barriers and streaks are upscaled well by the technique.

Keywords: upscaling, subgrid, numerical Greens functions, porous media, heterogeneity

1. Introduction

In a typical subsurface flow simulation, one is confronted with the problem of resolving extremely small scale features in the system or solution over very large spatial domains and over long time intervals. Direct simulation of all the relevant fine scale details is generally avoided as being too computationally expensive. Rather, some large scale averaging [27, 14] or homogenization [1, 16] of the fine scale system replaces it by an equivalent (in some sense) coarse scale model. Such an upscaling of information from the fine to the coarse scale smears out the solution so that one looses fine scale details. This is reasonable in certain cases, but in others it completely obscures the solution.

More recently, attempts have been made to capture the fine scale behavior of the solution directly on coarser grids. The multiscale finite element method [17], the residual free bubble techniques [18, 19, 9], certain domain-decomposition techniques [26, 31], and a-posteriori modeling techniques [21, 22] are examples of this idea. Each can be viewed as a subgrid technique in the sense that each attempts to resolve scales

below the coarse grid scale, by doing a significant amount of local work that contributes to a global problem defined only on a coarse grid.

In [6] and [3] a new approach to upscaling an elliptic partial differential equation was introduced that involves the decomposition of the solution operator into two pieces. In these two papers, the method is described in general terms, and numerical tests are given that demonstrate the overall speed and convergence properies of the method. Applications to groundwater contaminant transport and petroleum simulation are given in [4, 5], wherein it is shown that the method has great potential to resolve fine scale effects in practical problems.

We pursue this numerical upscaling technique in this paper by discussing in rather complete detail its implementation. A straightforward implementation of the method would give rise to certain computational complexities; however, as we show below, these can be easily avoided. Additional and more stringent numerical tests are presented by applying the technique to two-phase problems with significant heterogeneity. Moreover, the modeling of wells using a standard Peaceman approach [24, 25] is discussed in this paper. A significant advantage of the subgrid technique is that we need make no assumptions about the physics; rather, we use data provided on the fine scale directly in our computation, and we use the fine scale representation of the solution in the evaluation of nonlinear functions.

A brief outline of the paper follows. In the next section, we formulate a model elliptic problem that we use to discuss our upscaling technique, and cast it in a mixed variational form so that the mass conservation equation is retained. Our mixed finite element spaces are carefully defined in the third section, involving a two-scale definition of the basis functions. One part is defined on a coarse computational grid, and the rest defined on the fine scale within the coarse elements themselves (this is the *subgrid* part of the functions). In the fourth section we define our mixed finite element method on the global fine scale grid. This is merely for conceptual purposes, as it cannot be solved efficiently, but it does show clearly that mass is conserved locally. In Section 5, we discuss in detail our two-scale decomposition and an efficient implementation algorithm. We first impose the scale separation inherent in our finite element spaces. Next we show how to solve the subgrid portion of the solution independently of the coarse scale, by using numerical Greens functions or influence functions. This results in a series of small local problems, one for each coarse element. They are easily solved (and parallelize naturally). We follow this by a modification of the coarse scale problem, which leads us to our upscaled equation defined on the coarse computational grid. Combining the coarse and subgrid parts of the solution leads us to our final solution defined on the fine scale.

In Section 6, we show how to apply our algorithm to two-phase immiscible, incompressible flow in a porous medium. We consider the system as a pressure equation coupled to a saturation equation. We need upscale only the former equation. Also discussed are fixed rate wells and the Peaceman well model [24, 25]. In Section 7 we give three numerical examples illustrating the performance of the upscaling technique on near-well behavior, permeability barriers, and high permeability streaks or fractures. These are three of the more difficult phenomena to model accurately on coarse grids. The final section summarizes our conclusions.

2. A Model Elliptic Equation

It is easier for exposition to consider a model problem: we modify it later to obtain an application to the equations describing two-phase flow. Let $\Omega \subset \mathbb{R}^3$ be a connected polygonal domain that represents the spatial extent of the porous medium, and consider the model elliptic problem for the pressure p and Darcy velocity $\mathbf{u}$

$$ap + \nabla \cdot \mathbf{u} = b \qquad \text{in } \Omega , \tag{1}$$

$$\mathbf{u} = -d(\nabla p - c) \quad \text{in } \Omega , \tag{2}$$

wherein we have the scalars $a \geq 0$ and b, vector c, and second order positive definite tensor d. These should be sufficiently nice functions so that the method can be defined. Decompose $\partial\Omega$ as $\partial\Omega = \bar{\Gamma}_N \cup \bar{\Gamma}_R$, where $\Gamma_N \cup \Gamma_R = \emptyset$, and let ν be the unit outer normal vector. To this differential problem we add the boundary conditions

$$\mathbf{u} \cdot \nu = g_N \qquad \text{on } \Gamma_N , \tag{3}$$

$$\alpha \mathbf{u} \cdot \nu = p - g_R \quad \text{on } \Gamma_R , \tag{4}$$

representing Neumann and Robin (and Dirichlet, if $\alpha = 0$) conditions for suitably nice functions g_N, g_R, and $\alpha \geq 0$. We assume that a unique and sufficiently regular solution to this system exists.

One special case arises. If a vanishes identically on all of Ω, which we express by writing $a \equiv 0$, and if $\Gamma_N = \partial\Omega$ (i.e., $\Gamma_R = \emptyset$), then it is well-known and follows from the divergence theorem that solvability requires the compatibility condition

$$\int_\Omega b(x) \, dx = \int_{\partial\Omega} g_N(x) \, ds(x) . \tag{5}$$

In this case, we obtain p only up to an arbitrary constant. In practice, this special case arises, and we must be careful to differentiate it and apply the compatibility condition and normalize the pressure.

Our method is based on a mixed variational form, so that we can maintain local conservation of mass. Let

$$H(\text{div}; \Omega) = \{\mathbf{v} \in (L^2(\Omega))^3 \ : \ \nabla \cdot \mathbf{v} \in L^2(\Omega)\}$$

denote the usual space, and let

$$H^g(\text{div}; \Omega) = \{\mathbf{v} \in H(\text{div}; \Omega) \ : \ \mathbf{v} \cdot \nu = g \text{ on } \Gamma_N\} \ .$$

We denote by $(\cdot, \cdot)_\omega$ the $L^2(\omega)$ inner-product (i.e., integration over ω), where in the notation we suppress ω when it is Ω.

The mixed variational problem corresponding to (1)–(4) is to find $\mathbf{u} \in H^{g_N}(\text{div}; \Omega)$ and $p \in L^2(\Omega)$ such that

$$(ap, w) + (\nabla \cdot \mathbf{u}, w) = (b, w) \qquad \text{for all } w \in L^2(\Omega) \ , \qquad (6)$$

$$(d^{-1}\mathbf{u}, \mathbf{v}) + (\alpha \mathbf{u} \cdot \nu, \mathbf{v} \cdot \nu)_{\Gamma_R} - (p, \nabla \cdot \mathbf{v})$$
$$= (c, \mathbf{v}) - (g_R, \mathbf{v} \cdot \nu)_{\Gamma_R} \qquad \text{for all } \mathbf{v} \in H^0(\text{div}; \Omega) \ . \quad (7)$$

Note that (3) is imposed as an essential condition and (4) is imposed weakly as a natural boundary condition. We can now describe our numerical upscaling approximation.

3. The Finite Element Spaces

In a mixed finite element method, finite element basis functions are used to approximate both the pressure p and the velocity $\mathbf{u}$. For our upscaling procedure, in principle we can use any set of appropriate mixed spaces. However for efficiency and accuracy, it appears that there is a natural choice, to which we restrict our attention. We use the lowest order Raviart-Thomas space, RT0 [28] to approximate on the subgrid level, and we approximate on the coarse level with the first order Brezzi-Douglas-Duràn-Fortin space, BDDF1 [10], defined for 3 dimensional elements (in 2 dimensions, the space is the Brezzi-Douglas-Marini space, BDM1 [11]). We remark that we could use RT0 on the course scale; however, the results would not be as impressive (see [6]).

To construct our two-scale mesh, first decompose Ω into a coarse conforming mesh $\mathcal{T}_H(\Omega)$ of tetrahedra or rectangular parallelepipeds of maximal element diameter H. We assume that no coarse element face intersects both Γ_N and Γ_R. Next, we further decompose each coarse element E_c into a subgrid conforming mesh $\mathcal{T}_h(E_c)$ of tetrahedra and/or rectangular parallelepipeds of maximal element diameter h. Then the fine mesh is

$$\mathcal{T}_h(\Omega) = \bigcup_{E_c \in \mathcal{T}_H(\Omega)} \mathcal{T}_h(E_c) \ .$$

Note that the fine mesh $T_h(\Omega)$ need not conform across coarse element boundaries, and that the element shapes can vary from one coarse element to the next. In 2-D, we can even mix triangles and rectangles. Moreover, by using the Piola transform, one can include tri- or bilinearly distorted rectangular parallelepipeds [30, 12].

In both the BDDF1 and RT0 spaces, the pressure is approximated by a piecewise discontinuous constant function. That is, the pressure is approximated on each coarse element by a constant value, no matter whether the element is a tetrahedron or a rectangular parallelepiped. We recall the definition of the velocity basis functions below, beginning with the definitions on a single mesh element.

3.1. THE VELOCITY BASIS FUNCTIONS ON A TETRAHEDRON

The velocities are easily defined for BDDF1 on a tetrahedron (or triangle for BDM1) as the full set of vectors with linear polynomial components. This gives a 12 dimensional space (or 6 in 2-D). The normal component on each face of these vector functions is clearly linear, so there are 3 basis functions per face (or 2 per edge in 2-D).

The velocities of the RT0 spaces comprise the subset

$$\tilde{\mathbf{v}} = (c_1 x + c_2, c_1 y + c_3, c_1 z + c_4) \ ,$$

where each c_i is an arbitrary constant. These functions have a constant normal component $\tilde{\mathbf{v}} \cdot \nu$ on each face [28], and they form a 4 dimensional space (In 2-D, simply omit the third component, leaving a 3 dimensional space.)

We choose a local basis for BDDF1 (or BDM1 in 2-D) and RT0 such that the normal component vanishes on every face but one of the tetrahedron.

3.2. THE VELOCITY BASIS FUNCTIONS ON A RECTANGULAR PARALLELEPIPED

Now consider the standard unit cube $[0, 1]^3$. There are 6 velocity basis functions common to RT0 and BDDF1, which have a constant, nonzero divergence, given by

$$\begin{aligned}
\tilde{\mathbf{v}}_1 &= (1 - x)\mathbf{e}_1 \ , & \tilde{\mathbf{v}}_2 &= x\mathbf{e}_1 \ , \\
\tilde{\mathbf{v}}_3 &= (1 - y)\mathbf{e}_2 \ , & \tilde{\mathbf{v}}_4 &= y\mathbf{e}_2 \ , \\
\tilde{\mathbf{v}}_5 &= (1 - z)\mathbf{e}_3 \ , & \tilde{\mathbf{v}}_6 &= z\mathbf{e}_3 \ .
\end{aligned}$$

There is one function for each face of the element, and each represents a unit flow either into or out of the element across that face, and no

flow across the other faces. The BDDF1 spaces have 12 additional basis functions, each with vanishing divergence, given by

$$\tilde{\mathbf{v}}_7 = (1-x)(2y-1)\mathbf{e}_1 + (y^2-y)\mathbf{e}_2 \,, \ \ \tilde{\mathbf{v}}_8 = x(2y-1)\mathbf{e}_1 + (y-y^2)\mathbf{e}_2 \,,$$
$$\tilde{\mathbf{v}}_9 = (x^2-x)\mathbf{e}_1 + (1-y)(2x-1)\mathbf{e}_2 \,, \tilde{\mathbf{v}}_{10} = (x-x^2)\mathbf{e}_1 + y(2x-1)\mathbf{e}_2 \,,$$
$$\tilde{\mathbf{v}}_{11} = (x^2-x)\mathbf{e}_1 + (1-z)(2x-1)\mathbf{e}_3 \,, \tilde{\mathbf{v}}_{12} = (x-x^2)\mathbf{e}_1 + z(2x-1)\mathbf{e}_3 \,,$$
$$\tilde{\mathbf{v}}_{13} = (1-x)(2z-1)\mathbf{e}_1 + (z^2-z)\mathbf{e}_3 \,, \tilde{\mathbf{v}}_{14} = x(2z-1)\mathbf{e}_1 + (z-z^2)\mathbf{e}_3 \,,$$
$$\tilde{\mathbf{v}}_{15} = (1-y)(2z-1)\mathbf{e}_2 + (z^2-z)\mathbf{e}_3 \,, \tilde{\mathbf{v}}_{16} = y(2z-1)\mathbf{e}_2 + (z-z^2)\mathbf{e}_3 \,,$$
$$\tilde{\mathbf{v}}_{17} = (y^2-y)\mathbf{e}_2 + (1-z)(2y-1)\mathbf{e}_3 \,, \tilde{\mathbf{v}}_{18} = (y-y^2)\mathbf{e}_2 + z(2y-1)\mathbf{e}_3 \,.$$

These basis functions represent no net flow across the element faces; they merely redistribute flow across the face from one side to the other. (The BDM1 spaces omit $\tilde{\mathbf{v}}_5$, $\tilde{\mathbf{v}}_6$, and $\tilde{\mathbf{v}}_{11}$ to $\tilde{\mathbf{v}}_{18}$, leaving only 8 total basis functions.)

For an arbitrary rectangular element $[0,h_1] \times [0,h_2] \times [0,h_3]$, we translate and scale these functions. The scaling is to simply replace x by x/h_1, etc., except for the terms involving a square in $\tilde{\mathbf{v}}_7$ to $\tilde{\mathbf{v}}_{18}$. These latter basis functions must be scaled so that the divergence remains zero. For example, $\tilde{\mathbf{v}}_7$ becomes

$$\tilde{\mathbf{v}}_7 = (1-x/h_1)(2y/h_2-1)\mathbf{e}_1 + ((y/h_2)^2 - y/h_2)h_2/h_1\mathbf{e}_2 \,.$$

Improper scaling can result in serious mass balance and approximation errors [4].

3.3. The velocity basis functions on Ω

The element basis functions are paired across element faces so that the normal velocity is continuous. For example, two rectangular elements that share an x face would have $\tilde{\mathbf{v}}_2$ on the left and $\tilde{\mathbf{v}}_1$ on the right, or $\tilde{\mathbf{v}}_8$ on the left and $\tilde{\mathbf{v}}_7$ on the right. Thus there are 3 basis functions per element face for BDDF1 (or 2 per edge in 2-D), and 1 for RT0, no matter whether the adjoining elements are tetrahedra or rectangular parallelepipeds.

Let $\mathbf{V}_H \subset H(\mathrm{div};\Omega)$ and $W_H \in L^2(\Omega)$ denote the BDDF1 mixed finite element space described above defined over $\mathcal{T}_H(\Omega)$.

For each coarse element $E_c \in \mathcal{T}_H(\Omega)$, let $\delta\mathbf{V}_h^*(E_c) \subset H(\mathrm{div};E_c)$ and $W_h(E_c) \in L^2(E_c)$ denote the RT0 space defined over $\mathcal{T}_h(E_c)$. These spaces do not piece together in a conforming way without additional conditions; however, to make them conforming would prevent us from localizing the subgrid approximation later. We therefore disallow normal fluxes on the subgrid element faces that are contained in ∂E_c:

$$\delta\mathbf{V}_h(E_c) = \{\mathbf{v} \in \delta\mathbf{V}_h^*(E_c) \ : \ \mathbf{v} \cdot \nu = 0 \text{ on } \partial E_c\} \,.$$

Now extend elements of each $\delta \mathbf{V}_h(E_c)$ to all of Ω by zero and let

$$\delta \mathbf{V}_h = \bigoplus_{E_c \in \mathcal{T}_H(\Omega)} \delta \mathbf{V}_h(E_c)$$

be the direct sum of the subgrid spaces over all coarse elements. Furthermore, let W_h be the direct sum of the $W_h(E_c)$, i.e., the space of piecewise discontinuous constants defined over the fine mesh $\mathcal{T}_h(\Omega)$.

Finally, let

$$\mathbf{V}_{H,h} = \mathbf{V}_H \oplus \delta \mathbf{V}_h \ , \tag{8}$$

which is easily seen to be a direct sum (i.e., the basis functions are linearly independent). Our finite element space defined over our composite fine mesh $\mathcal{T}_h(\Omega)$ is given by $\mathbf{V}_{H,h} \times W_h$, which is a mixture of BDDF1 and RT0 basis functions. As illustrated in the 2-D rectangular mesh of Fig. 1, the velocity has 2 fluxes on each coarse element face representing flow between the elements that varies linearly over the edge, and a single constant flux across fine grid edges that lie within the coarse elements.
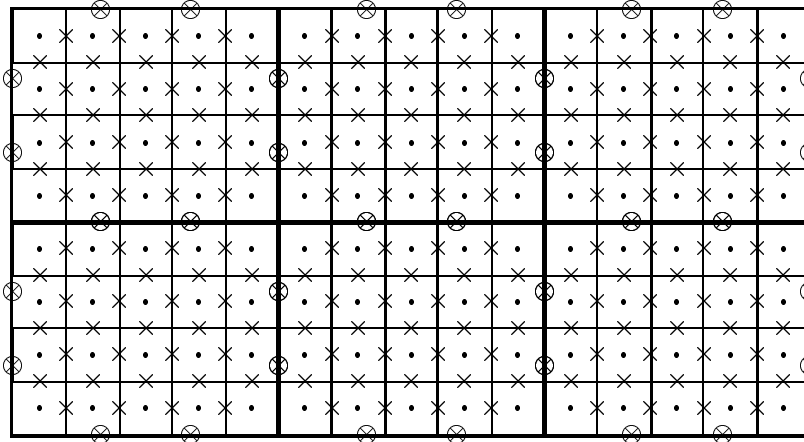
Figure 1. A 2-D mesh of 15×8 fine grid elements decomposed into a 3×2 coarse grid with 5×4 subgrid elements per coarse element. The dots represent the pressure values, one per fine element. The crosses represent the edge velocity fluxes. The circled crosses apply to the coarse grid edges, and represent linear flux variation. The other crosses represent constant fluxes across the subgrid edges internal to the coarse elements.

In essence, the RT0 subgrid approximating spaces have homogeneous Neumann boundary conditions on the coarse element boundaries. This localizes the subgrid problems, making them disjoint from each other (but *not* the coarse scale problem). All net flux across a coarse

element face goes through the coarse scale functions. To compensate for the coarseness of this restriction, higher order accurate basis functions have been employed. Thus we have achieved both good resolution and localization of the subgrid basis functions.

4.   The Mixed Finite Element Method

To impose the boundary conditions (3)–(4), we assume that no coarse element face intersects both Γ_N and Γ_R. Moreover, we define the trace space on $\partial\Omega$ by
$$\Lambda_H = \mathbf{V}_H \cdot \nu = \mathbf{V}_{H,h} \cdot \nu \ ,$$
which are simply piecewise discontinuous linear polynomials. Now define the orthogonal L^2-projection operator $\mathcal{P}_{\Lambda_H} : L^2(\partial\Omega) \to \Lambda_H$ by
$$(\mathcal{P}_{\Lambda_H} g - g, \mathbf{v} \cdot \nu)_{\partial\Omega} = 0 \quad \text{for all } \mathbf{v} \in \mathbf{V}_H \ ,$$
and let
$$\mathbf{V}_H^g = \{\mathbf{v} \in \mathbf{V}_H \ : \ \mathbf{v} \cdot \nu = \mathcal{P}_{\Lambda_H} g \text{ on } \Gamma_N\} \ ,$$
$$\mathbf{V}_{H,h}^g = \{\mathbf{v} \in \mathbf{V}_{H,h} \ : \ \mathbf{v} \cdot \nu = \mathcal{P}_{\Lambda_H} g \text{ on } \Gamma_N\} \ .$$

That is, on each element face of Γ_N, $\mathbf{v} \cdot \nu$ is the L^2-projection of g into the linear polynomials.

Our finite element method is analogous to (6)–(7): Find $\mathbf{U} \in \mathbf{V}_{H,h}^{g_N}$ and $P \in W_h$ such that

$$(aP, w) + (\nabla \cdot \mathbf{U}, w) = (b, w) \qquad\qquad \text{for all } w \in W_h \ , \qquad (9)$$
$$(d^{-1}\mathbf{U}, \mathbf{v}) + (\alpha\mathbf{U} \cdot \nu, \mathbf{v} \cdot \nu)_{\Gamma_R} - (P, \nabla \cdot \mathbf{v})$$
$$\qquad = (c, \mathbf{v}) - (g_R, \mathbf{v} \cdot \nu)_{\Gamma_R} \qquad\qquad \text{for all } \mathbf{v} \in \mathbf{V}_{H,h}^0 \ . \quad (10)$$

Note that the conservation equation (9) is retained in the system, and that $w \in W_h$ enforces conservation locally over each fine element.

Theorem 4.1. *If $a \not\equiv 0$ or $\Gamma_R \neq \emptyset$, then there is a unique solution to the finite element scheme (9)–(10). Moreover, if $a \equiv 0$ and $\Gamma_R = \emptyset$ and the compatibility condition (5) holds, then there is again a solution, and $\mathbf{U}$ is unique and P is unique up to a constant.*

In the latter case, P is unique provided we also impose a normalization condition such as

$$\int_\Omega P(x)\,dx = 0 \ . \qquad\qquad (11)$$

Before presenting the proof, we need two lemmas. The first is well known.

Lemma 4.1. *Suppose that $\omega \subset \mathbb{R}^3$ is a connected domain with a conforming mesh $\mathcal{T}$ of tetrahedra or rectangular parallelepipeds, and $\tilde{\mathbf{V}} \times \tilde{W}$ is the RT0 space defined over $\mathcal{T}$. Suppose also that $\gamma \subset \partial\omega$, no element of $\mathcal{T}$ intersects both γ and its complement, and*

$$\tilde{\mathbf{V}}^0 = \{\mathbf{v} \in \tilde{\mathbf{V}} \: : \: \mathbf{v} \cdot \nu = 0 \text{ on } \gamma\} \ .$$

Given $w \in \tilde{W}$, there is a $\mathbf{v} \in \tilde{\mathbf{V}}^0$ such that

$$\nabla \cdot \mathbf{v} = w \ ,$$

provided that if $\gamma = \partial\omega$, the average of w vanishes on ω.

Lemma 4.2. *If $\bar{\Gamma}_N \neq \partial\Omega$, then*

$$\nabla \cdot \mathbf{V}_{H,h}^0 = W_h \ .$$

If $\bar{\Gamma}_N = \partial\Omega$, then

$$\nabla \cdot \mathbf{V}_{H,h}^0 = W_h^0 \equiv \left\{ w \in W_h \: : \: \int_\Omega w(x)\,dx = 0 \right\} \ .$$

Proof. Clearly by construction

$$\nabla \cdot \mathbf{V}_{H,h}^0 \subset W_h \ ,$$

and, if $\bar{\Gamma}_N = \partial\Omega$, $\nabla \cdot \mathbf{V}_{H,h}^0 \subset W_h^0$. It remains to show that given $w \in W_h$ (or W_h^0 when $\bar{\Gamma}_N = \partial\Omega$), there is $\mathbf{v} \in \mathbf{V}_{H,h}^0$ such that $\nabla \cdot \mathbf{v} = w$. This follows from the previous lemma as follows. First construct $w_H \in W_H$ by defining w_H on each coarse element E_c as the average of w:

$$w_H = \mathcal{P}_{W_H} w \ ,$$

where we define the orthogonal L^2-projection operator $\mathcal{P}_{W_H} : L^2(\Omega) \to W_H$ by

$$(\mathcal{P}_{W_H} g - g, \xi) = 0 \quad \text{for all } \xi \in W_H \ .$$

Then Lemma 4.1 gives $\mathbf{v}_c$ in the RT0 part of $\mathbf{V}_H^0 \subset \mathbf{V}_{H,h}^0$ defined over the coarse mesh $\mathcal{T}_H$ such that

$$\nabla \cdot \mathbf{v}_c = w_H = \mathcal{P}_{W_H} w \ .$$

Next we define

$$\delta w = w - w_H \ ,$$

and note that on each coarse element E_c, δw has zero average value. Thus Lemma 4.1 gives us $\delta \mathbf{v}$ in RT0 defined over the mesh $\mathcal{T}_h(E_c)$ with vanishing normal component such that $\nabla \cdot \delta \mathbf{v} = \delta w$. Adding the pieces together gives $\mathbf{v} = \mathbf{v}_c + \delta \mathbf{v} \in \mathbf{V}_{H,h}^0$ such that $\nabla \cdot \mathbf{v} = w$. □

Proof of Theorem 4.1. The proof follows from the equivalence of existence and uniqueness for a square finite dimensional linear system. Uniqueness follows from uniqueness at zero, so set g_N, g_R, b, and c to zero in (9)–(10) and substitute for $(\mathbf{v}, w)$ any solution $(\mathbf{U}, P) \in \mathbf{V}_{H,h}^0 \times W_h$. The sum of the two equations is

$$(aP, P) + (d^{-1}\mathbf{U}, \mathbf{U}) + (\alpha\mathbf{U} \cdot \nu, \mathbf{U} \cdot \nu)_{\Gamma_R} = 0 \ . \tag{12}$$

Since a and α are nonnegative, and d, and thus also d^{-1}, is positive definite, we conclude that $\mathbf{U} = 0$.

We return to (10), which in our case is simply

$$(P, \nabla \cdot \mathbf{v}) = 0 \quad \text{for all } \mathbf{v} \in \mathbf{V}_{H,h}^0 \ ,$$

and select by Lemma 4.2 a test function $\mathbf{v} \in \mathbf{V}_{H,h}^0$ such that $\nabla \cdot \mathbf{v} = P$ if $\Gamma_R \neq \emptyset$ and $\nabla \cdot \mathbf{v} = P - \bar{P}$ if $\Gamma_R = \emptyset$, where $\bar{P}$ is the average of P over Ω. In the former case, we conclude that $P = 0$. In the latter case, we conclude only that $P = \bar{P}$ is constant. If $a \not\equiv 0$, our previous estimate $(aP, P) = 0$ from (12) verifies that indeed $P = 0$; otherwise, the normalization condition (11) is applied and gives the same conclusion.

Thus in all cases we have uniqueness at zero, and so the theorem follows. $\qquad\qquad\qquad\qquad\qquad\qquad\qquad\qquad\qquad\qquad\qquad\square$

5. Implementation

If the finite element method is implemented as stated in the previous section, there is no computational advantage, since it is essentially defined as a fine scale problem. We need to reorganize the computation so that it upscales from the subgrid scale to the coarse scale, by exploiting the two-scale decomposition (8).

5.1. Scale separation

Since $\mathbf{V}_{H,h} = \mathbf{V}_H \oplus \delta\mathbf{V}_h$, we can decompose $\mathbf{U}$ uniquely into

$$\mathbf{U} = \mathbf{U}_H + \delta\mathbf{U} \ , \tag{13}$$

where $\mathbf{U}_H \in \mathbf{V}_H$ and $\delta\mathbf{U} \in \delta\mathbf{V}_h$.

We remark that W_H and W_h are not linearly independent (in fact, $W_H \subset W_h$). We could rectify this problem by defining

$$\delta W_h = W_H^\perp = \{w \in W_h \ : \ (w, w_H) = 0 \text{ for all } w_H \in W_H\} \ .$$

Then indeed

$$W_h = W_H \oplus \delta W_h \ .$$

While this is a conceptually useful construction, it turns out that it is computationally inconvenient, since each $\delta w \in \delta W_h$ is supported on at least two subgrid elements. Thus we will continue to use the full space W_h and deal with the nonuniqueness another way.

For future reference, note that $\nabla \cdot \delta \mathbf{V}_h = \delta W_h = W_H^\perp$ by Lemma 4.1. That is, we have the orthogonality

$$(\nabla \cdot \delta \mathbf{v}, w_H) = 0 \quad \text{for all } \delta \mathbf{v} \in \delta \mathbf{V}_h \text{ and } w_H \in W_H \ . \tag{14}$$

5.2. The subgrid scale

If we restrict to the subgrid scale test functions in (9)–(10) and use the decomposition (13), we obtain the series of subgrid problems, one for each coarse element E_c,

$$
\begin{aligned}
(aP, w)_{E_c} &+ (\nabla \cdot \delta \mathbf{U}, w)_{E_c} \\
&= (b, w)_{E_c} - (\nabla \cdot \mathbf{U}_H, w)_{E_c} \qquad \text{for all } w \in W_h(E_c) \ , \tag{15} \\
(d^{-1} \delta \mathbf{U}, \delta \mathbf{v})_{E_c} &- (P, \nabla \cdot \delta \mathbf{v})_{E_c} \\
&= (c, \delta \mathbf{v})_{E_c} - (d^{-1} \mathbf{U}_H, \delta \mathbf{v})_{E_c} \quad \text{for all } \delta \mathbf{v} \in \delta \mathbf{V}_h(E_c) \ . \tag{16}
\end{aligned}
$$

5.2.1. The subgrid scale operator when $a \not\equiv 0$ on E_c

We continue the development assuming that a is positive on some part of the coarse element E_c.

Lemma 5.1. *Suppose that* $\mathbf{U}_H \in \mathbf{V}_H^{g_N}$ *is given. If* $a \not\equiv 0$ *on* E_c*, then there is a unique solution* $(\delta \mathbf{U}, P) \in \delta \mathbf{V}_h(E_c) \times W_h(E_c)$ *to* (15)–(16).

The proof is similar to that for Theorem 4.1, and so it is omitted.

Thus we have a well-defined subgrid solution operator taking $\mathbf{V}_H^{g_N}$ to $\delta \mathbf{V}_h \times W_h$. This operator is affine: it can be represented as the sum of a constant operator and a linear one. Moreover, the operator is locally defined; that is, it is the sum of operators defined on each E_c. These local operators are defined on the low dimensional space $\mathbf{V}_H(E_c)$, which has dimension 18 on a rectangular parallelepiped and 12 on a tetrahedron. We can exploit this special structure to upscale the problem and thereby obtain a computationally efficient scheme. This is because we need only understand the action of the operator on a basis of $\mathbf{V}_H(E_c)$. Let $\{\mathbf{v}_j\}_{j \geq 1}$ be a basis for $\mathbf{V}_H(E_c)$.

Define $(\delta\mathbf{U}_0, P_0) \in \delta\mathbf{V}_h(E_c) \times W_h(E_c)$ satisfying

$$(aP_0, w)_{E_c} + (\nabla \cdot \delta\mathbf{U}_0, w)_{E_c} = (b, w)_{E_c} \quad \text{for all } w \in W_h(E_c) \, , \qquad (17)$$

$$(d^{-1}\delta\mathbf{U}_0, \delta\mathbf{v})_{E_c} - (P_0, \nabla \cdot \delta\mathbf{v})_{E_c}$$
$$= (c, \delta\mathbf{v})_{E_c} \qquad\qquad\qquad\qquad \text{for all } \delta\mathbf{v} \in \delta\mathbf{V}_h(E_c) \, . \quad (18)$$

This is the constant part of our subgrid solution operator. Next, for each basis function $\mathbf{v}_j \in \mathbf{V}_H(E_c)$, let $(\delta\mathbf{U}_j, P_j) \in \delta\mathbf{V}_h(E_c) \times W_h(E_c)$ satisfy

$$(aP_j, w)_{E_c} + (\nabla \cdot \delta\mathbf{U}_j, w)_{E_c}$$
$$= -(\nabla \cdot \mathbf{v}_j, w)_{E_c} \qquad\qquad \text{for all } w \in W_h(E_c) \, , \qquad (19)$$

$$(d^{-1}\delta\mathbf{U}_j, \delta\mathbf{v})_{E_c} - (P_j, \nabla \cdot \delta\mathbf{v})_{E_c}$$
$$= -(d^{-1}\mathbf{v}_j, \delta\mathbf{v})_{E_c} \qquad\qquad \text{for all } \delta\mathbf{v} \in \delta\mathbf{V}_h(E_c) \, . \qquad (20)$$

This gives the action of the linear part of our subgrid solution operator acting on the basis of our space $\mathbf{V}_H(E_c)$.

In general, for any $\mathbf{U}_H \in \mathbf{V}_H$, $\mathbf{U}_H$ restricted to E_c is simply the linear combination

$$\mathbf{U}_H|_{E_c} = \sum_j \beta_j \mathbf{v}_j \, , \qquad\qquad (21)$$

for some coefficients β_j. Moreover, it is easy to verify that the solution to (15)–(16) is

$$\delta\mathbf{U} = \sum_j \beta_j \delta\mathbf{U}_j + \delta\mathbf{U}_0 \, , \qquad\qquad (22)$$

$$P = \sum_j \beta_j P_j + P_0 \, . \qquad\qquad (23)$$

That is, the subgrid solution operator is decomposed into the constant piece $(\delta\mathbf{U}_0, P_0)$ and a small linear combination of the $(\delta\mathbf{U}_j, P_j)$.

We remark that $(\delta\mathbf{U}_j, P_j)$ is the solution to the unit disturbance $\mathbf{v}_j$ to the system, where "unit" is defined with respect to the finite dimensional domain of the operator. Since any solution can be generated from these, we can consider these special solutions as *numerical Greens functions*. They are also called *influence functions*.

5.2.2. *Renormalization of the subgrid scale operator when $a \not\equiv 0$ on E_c*
For consistency with the $a \equiv 0$ case, and for ease of implementation later, we renormalize P_i as $\delta P_i \in W_h(E_c)$. Let $|E_c|$ denote the volume of $|E_c|$ and define

$$\delta P_0 = P_0 - \frac{1}{|E_c|} \int_{E_c} P_0(x)\, dx \, , \qquad\qquad (24)$$

and define

$$\delta P_j = P_j - \frac{\displaystyle\int_{E_c} a(x) P_0(x) \, dx}{\displaystyle\int_{E_c} a(x) \, dx}, \ \ j = 1, 2, \ldots . \tag{25}$$

Let

$$\delta P = \sum_j \beta_j \delta P_j + \delta P_0 \ , \tag{26}$$

and note that on E_c,

$$P = P_H + \delta P \tag{27}$$

for some $P_H \in W_H$.

For future reference, our normalization makes the following integrals vanish:

$$(\delta P_0, w_H) = (a\delta P_j, w_H) = 0 \quad \text{for all } w_H \in W_H, \ j = 1, 2, \ldots . \tag{28}$$

5.2.3. *The subgrid scale operator when $a \equiv 0$ on E_c*

When $a \equiv 0$ on the coarse element E_c, there may be no solution to (15)–(16) since the compatibility condition may fail to hold. Thus we must modify our approach.

For the constant part of the subgrid operator, define $(\delta\mathbf{U}_0, \delta P_0) \in \delta\mathbf{V}_h(E_c) \times W_h(E_c)$ satisfying

$$(\nabla \cdot \delta\mathbf{U}_0, w)_{E_c} = (b - \mathcal{P}_{W_H} b, w)_{E_c} \quad \text{for all } w \in W_h(E_c) \ , \tag{29}$$

$$(d^{-1}\delta\mathbf{U}_0, \delta\mathbf{v})_{E_c} - (\delta P_0, \nabla \cdot \delta\mathbf{v})_{E_c}$$
$$= (c, \delta\mathbf{v})_{E_c} \qquad\qquad \text{for all } \delta\mathbf{v} \in \delta\mathbf{V}_h(E_c) \ , \tag{30}$$

$$\int_\Omega \delta P_0(x) \, dx = 0 \ . \tag{31}$$

For each basis function $\mathbf{v}_j \in \mathbf{V}_H(E_c)$, let $(\delta\mathbf{U}_j, \delta P_j) \in \delta\mathbf{V}_h(E_c) \times W_h(E_c)$ satisfy

$$(\nabla \cdot \delta\mathbf{U}_j, w)_{E_c} = 0 \qquad\qquad \text{for all } w \in W_h(E_c) \ , \tag{32}$$

$$(d^{-1}\delta\mathbf{U}_j, \delta\mathbf{v})_{E_c} - (\delta P_j, \nabla \cdot \delta\mathbf{v})_{E_c}$$
$$= -(d^{-1}\mathbf{v}_j, \delta\mathbf{v})_{E_c} \qquad\qquad \text{for all } \delta\mathbf{v} \in \delta\mathbf{V}_h(E_c) \ , \tag{33}$$

$$\int_\Omega \delta P_j(x) \, dx = 0 \ . \tag{34}$$

Because of the homogeneous Neumann boundary condition imposed on the space $\delta\mathbf{V}_h(E_c)$, we see that there is a redundancy in (29) and (32); that is, any constant test function w_c gives the tautology $(\nabla \cdot \delta\mathbf{v}, w_c)_{E_c} = 0$. To maintain a square linear system, we therefore replace any single such equation by our normalization condition on the pressure.

Lemma 5.2. *Suppose that* $\mathbf{U}_H \in \mathbf{V}_H^{g_N}$ *is given. Then (29)–(31) and (32)–(34) have unique solutions.*

Again the proof is similar to that for Theorem 4.1 and omitted.

If we define $\delta\mathbf{U}$ by (22) and δP by (26), and if we recall (21), then we see that $(\delta\mathbf{U}, \delta P) \in \delta\mathbf{V}_h(E_c) \times W_h(E_c)$ satisfy

$$(\nabla \cdot \delta\mathbf{U}, w)_{E_c} = (b - \mathcal{P}_{W_H} b, w)_{E_c} \quad \text{for all } w \in W_h(E_c) \ ,$$

$$(d^{-1}\delta\mathbf{U}, \delta\mathbf{v})_{E_c} - (\delta P, \nabla \cdot \delta\mathbf{v})_{E_c}$$
$$= (c, \delta\mathbf{v})_{E_c} - (d^{-1}\mathbf{U}_H, \delta\mathbf{v})_{E_c} \quad \text{for all } \delta\mathbf{v} \in \delta\mathbf{V}_h(E_c) \ .$$

However, if we restrict to $w \in W_H$ in (9), take $a \equiv 0$, and recall the orthogonality (14), then we see that in fact

$$\nabla \cdot \mathbf{U}_H = \mathcal{P}_{W_H} b \ ,$$

so, given $\mathbf{U}_H$ and P_H, $(\delta\mathbf{U}, P)$ is the solution to (15)–(16), with (27) defining P.

5.3. The upscaled equation

We return to the coarse scale. Restrict to coarse scale test functions in (9)–(10) and use the decomposition (13) and (27) to obtain

$$\begin{aligned}(a(P_H &+ \delta P), w_H) + (\nabla \cdot \mathbf{U}_H, w_H) \\ &= (b, w_H) \qquad\qquad\qquad \text{for all } w_H \in W_H \ , \qquad (35) \\ (d^{-1}(\mathbf{U}_H &+ \delta\mathbf{U}), \mathbf{v}_H) + (\alpha\mathbf{U}_H \cdot \nu, \mathbf{v}_H \cdot \nu)_{\Gamma_R} - (P_H + \delta P, \nabla \cdot \mathbf{v}_H) \\ &= (c, \mathbf{v}_H) - (g_R, \mathbf{v}_H \cdot \nu)_{\Gamma_R} \quad \text{for all } \mathbf{v}_H \in \mathbf{V}_H^0 \ , \qquad (36)\end{aligned}$$

wherein we used the orthogonality (14) to remove a term in the conservation equation.

Substituting (26) into (35) and exploiting our normalization (28) if $a \not\equiv 0$, we obtain

$$(aP_H, w_H) + (\nabla \cdot \mathbf{U}_H, w_H) = (b - a\delta P_0, w_H) \quad \text{for all } w_H \in W_H \ , \tag{37}$$

which only involves the coarse unknowns P_H and $\mathbf{U}_H$, since δP_0 is fixed. Our task now is to simplify the Darcy equation, since it involves implicitly the basis coefficients of $\mathbf{U}_H$ through the terms $\delta \mathbf{U}$ and δP.

We need to introduce some additional notation relating global and local indexing. Let $\ell = 1, 2, \ldots$ index the coarse vector basis functions of $\mathbf{V}_H$, so that

$$\mathbf{U}_H = \sum_\ell \beta_\ell \mathbf{v}_\ell \tag{38}$$

for some coefficients β_ℓ. Except near $\partial\Omega$, each $\mathbf{v}_\ell$ is supported on two coarse elements, E_c^1 and E_c^2, for which the normal flux of $\mathbf{v}_\ell$ is associated with the common face $\partial E_c^1 \cap \partial E_c^2$. Then we have that

$$\mathbf{U}_H = \sum_\ell \beta_\ell (\mathbf{v}_\ell|_{E_c^1} + \mathbf{v}_\ell|_{E_c^2}) \ .$$

Now $\mathbf{v}_\ell|_{E_c^i}$ gives rise to a subgrid numerical Greens function $\delta \mathbf{U}_j^{E_c^i}$ on E_c^i for each $i = 1, 2$. Given the coefficients β_ℓ, we construct $\delta \mathbf{U} \in \delta \mathbf{V}_h$ globally as

$$\delta \mathbf{U} = \delta \mathbf{U}_0 + \sum_\ell \beta_\ell (\delta \mathbf{U}_j^{E_c^1} + \delta \mathbf{U}_j^{E_c^2}) \ ,$$

Let us define

$$\delta \mathbf{U}_\ell = \delta \mathbf{U}_j^{E_c^1} + \delta \mathbf{U}_j^{E_c^2} \in \delta \mathbf{V}_h \ ,$$

so that we can write more simply

$$\delta \mathbf{U} = \delta \mathbf{U}_0 + \sum_\ell \beta_\ell \delta \mathbf{U}_\ell \ . \tag{39}$$

Similarly, we construct

$$\delta P = \delta P_0 + \sum_\ell \beta_\ell \delta P_\ell \ , \tag{40}$$

where

$$\delta P_\ell = \delta P_j^{E_c^1} + \delta P_j^{E_c^2} \ .$$

5.3.1. *The nonsymmetric upscaled problem*
Substituting the expansion (38), (39), and (40) into (36), and using (28) and restricting to test functions in our basis results in

$$\sum_\ell \beta_\ell \{ (d^{-1}(\mathbf{v}_\ell + \delta \mathbf{U}_\ell), \mathbf{v}_m) + (\alpha \mathbf{v}_\ell \cdot \nu, \mathbf{v}_m \cdot \nu)_{\Gamma_R}$$

$$- (\delta P_\ell, \nabla \cdot \mathbf{v}_m) \} - (P_H, \nabla \cdot \mathbf{v}_m)$$

$$= -(d^{-1}\delta \mathbf{U}_0, \mathbf{v}_m) + (c, \mathbf{v}_m) - (g_R, \mathbf{v}_m \cdot \nu)_{\Gamma_R}$$

$$\text{for all } m = 1, 2, \ldots \ . \tag{41}$$

5.3.2. *The symmetric upscaled problem*

Our model problem is symmetric. We symmetrize our matrix problem next, possibly for use with a conjugate gradient solver. We do this by adding some of the subgrid equations; equivalently, we could return to (10) and use test functions $\mathbf{v}_m + \delta\mathbf{U}_m$. Assume that $a \not\equiv 0$, since the other case is easier.

In (20), substitute the test function $\delta\mathbf{v} = \delta\mathbf{U}_m$ to obtain that

$$(d^{-1}(\mathbf{v}_j + \delta\mathbf{U}_j), \delta\mathbf{U}_m) - (\delta P_j, \nabla \cdot \delta\mathbf{U}_m) = (P_j - \delta P_j, \nabla \cdot \delta\mathbf{U}_m) = 0 \ ,$$

by (14). Next, replacing j by m in (19) and testing with $w = \delta P_j$ gives

$$(\delta P_j, \nabla \cdot (\mathbf{v}_m + \delta\mathbf{U}_m)) = -(a\delta P_j, P_m) = -(a\delta P_j, \delta P_m) \ ,$$

using (28). Replace j by ℓ, multiply by β_ℓ, and add to (41) to obtain the result

$$\begin{aligned}
\sum_\ell \beta_\ell \{ & (d^{-1}(\mathbf{v}_\ell + \delta\mathbf{U}_\ell), \mathbf{v}_m + \delta\mathbf{U}_m) + (\alpha\mathbf{v}_\ell \cdot \nu, \mathbf{v}_m \cdot \nu)_{\Gamma_R} \\
& + (a\delta P_\ell, \delta P_m) \} - (P_H, \nabla \cdot \mathbf{v}_m) \\
= & -(d^{-1}\delta\mathbf{U}_0, \mathbf{v}_m) + (c, \mathbf{v}_m) - (g_R, \mathbf{v}_m \cdot \nu)_{\Gamma_R} \\
& \text{for all } m = 1, 2, \dots \ ,
\end{aligned} \tag{42}$$

which is symmetric. If $a \equiv 0$, the same result is obtained from (32)–(34).

5.3.3. *The upscaled problem when $a > 0$ on Ω*

When $a > 0$ on Ω, or more generally when it is known that $a \not\equiv 0$ on each coarse element E_c, we need neither the renormalization step nor (37), since P is fully defined implicitly by $\mathbf{U}_H$. This case arises for strictly parabolic equations. The same equations (41) and (42) result, if we merely replace P_H by P_0 and each δP_i by P_i.

5.4. THE SOLUTION ALGORITHM

We summarize the solution algorithm outlined above. It has three steps.

5.4.1. *The case when $a \equiv 0$ on at least one coarse element*

Assuming $a \equiv 0$ on at least one element E_c, we cannot solve for all of P in the subgrid step.

Step 1–Subgrid scale. We loop over the coarse elements E_c. We obtain in this step δP_0 and the numerical Greens functions δP_j, $j = 1, 2, \dots$, as follows. If $a \not\equiv 0$ on E_c, we solve (17)–(18) and (19)–(20), and renormalize via (24)–(25). If $a \equiv 0$ on E_c, we instead solve (29)–(31) and (32)–(34).

These problems generate the same finite element matrix, and vary only in their "right-hand-side" vector. They are also relatively small linear systems, so a direct solver can be used here effectively. A unique solution exists by Lemmas 5.1 and 5.2. Moreover, this step parallelizes naturally.

Step 2—Coarse scale. Because we allow for the possibility that $a \equiv 0$ on a coarse element, we could not determine P completely from the subgrid computation. Thus we must solve the coarse scale conservation equation (37). This is combined with the Darcy Law equation, either the nonsymmetric (41) or the symmetric (42). When β_ℓ is associated with a face on Γ_N, we use $\mathcal{P}_{\Lambda_H} g_N$ to set its value. Then this system has a unique solution $(\mathbf{U}_H, P_H) \in \mathbf{V}_H^{g_N} \times W_H$, by Theorem 4.1, since the subgrid is well defined. We are essentially solving a Shur complement problem extracted from the full fine scale problem (9)–(10).

This step is essentially equivalent in work and complexity to a non-upscaled coarse problem, similar in form to (9)–(10), albeit solved using the BDDF1 mixed finite element spaces. The main difference is in the finite element matrix related to $\mathbf{U}_H$, for which the (m, ℓ) entry is, in the symmetric case,

$$(d^{-1}(\mathbf{v}_\ell + \delta \mathbf{U}_\ell), \mathbf{v}_m + \delta \mathbf{U}_m) + (\alpha \mathbf{v}_\ell \cdot \nu, \mathbf{v}_m \cdot \nu)_{\Gamma_R} + (a \delta P_\ell, \delta P_m) \ ,$$

rather than simply

$$(d^{-1} \mathbf{v}_\ell, \mathbf{v}_m) + (\alpha \mathbf{v}_\ell \cdot \nu, \mathbf{v}_m \cdot \nu)_{\Gamma_R} \ .$$

This requires a change to the element integration routine. The only other modifications are to the coefficient c, which becomes $c - d^{-1} \delta \mathbf{U}_0$, and the function b, which becomes $b - a \delta P_0$. Of course, the finite element integrations must be performed on the fine scale.

Mixed finite element methods result in linear systems of saddle point form, with both positive and negative eigenvalues. One can use the Lagrange multiplier solution procedure [8] to avoid the saddle-point problem.

We use the symmetric system (42) transformed by the introduction of Lagrange multipliers [8] to obtain a symmetric, positive definite system, and then solve it via a conjugate gradient iterative procedure. A domain decomposition procedure [15] could be used to parallelize this computation.

Step 3—Fine scale. One advantage of our technique is that we recover a fine scale representation of our solution. The last step is to construct $\mathbf{U} \in \mathbf{V}_{H,h}^{g_N}$ through (39) and (13), and $P \in W_h$ through (40) and (27).

5.4.2. *The case when $a > 0$ on Ω*

When $a > 0$ on Ω (or $a \not\equiv 0$ on each E_c), we have a somewhat simpler procedure.

Step 1–Subgrid scale. We loop over the coarse elements E_c, and solve (17)–(18) and (19)–(20) for P_0 and the numerical Greens functions P_j, $j = 1, 2, \dots$.

Step 2—Coarse scale. We solve only the Darcy equation, since the subgrid fully determines P. We solve the equations (41) or (42), wherein we replace P_H by P_0 and each δP_i by P_i, and set any β_ℓ determined by $\mathcal{P}_{\Lambda_H} g_N$.

Step 3—Fine scale. We construct $\mathbf{U} \in \mathbf{V}_{H,h}^{g_N}$ by (39) and (13), and $P \in W_h$ by (23).

5.5. A REMARK ON NONLINEAR PROBLEMS

Nonlinear problems can be numerically upscaled after applying Newton linearization. To illustrate, suppose that instead of the variational problem (6)–(7) we have the nonlinear version

$$(a(p)p, w) + (\nabla \cdot \mathbf{u}, w) = (b(p), w) \ ,$$
$$(d^{-1}(p)\mathbf{u}, \mathbf{v}) - (p, \nabla \cdot \mathbf{v}) = (c(p), \mathbf{v}) \ ,$$

wherein for simplicity of exposition we assume homogeneous Neumann boundary conditions. Under appropriate hypotheses on the nonlinearities, we obtain a solution from an initial guess $(p^0, \mathbf{u}^0)$ by iterating on k to find $p^{k+1} = p^k + q^k$ and $\mathbf{u}^{k+1} = \mathbf{u}^k + \psi^k$ after solving for (q^k, ψ^k) satisfying the linearized equations

$$((a(p^k) + Da(p^k)p^k - Db(p^k))q^k, w) + (\nabla \cdot \psi^k, w)$$
$$= (b(p^k) - a(p^k)p^k - \nabla \cdot \mathbf{u}^k, w) \ ,$$
$$(d^{-1}(p^k)\psi^k, \mathbf{v}) - (q^k, \nabla \cdot \mathbf{v}) + ((Dd^{-1}(p^k)\mathbf{u}^k - Dc(p^k))q^k, \mathbf{v})$$
$$= (c(p^k) - d^{-1}(p^k)\mathbf{u}^k, \mathbf{v}) + (p^k, \nabla \cdot \mathbf{v}) \ .$$

This linearized system has the same form as (6)–(7), with modified coefficients, except for the introduction of the nonsymmetric third term in the second equation of the form

$$(\mathbf{e}p, \mathbf{v}) \approx (\mathbf{e}p_h, \mathbf{v}) = (\mathbf{e}(p_H + \delta p), \mathbf{v}_c + \delta \mathbf{v}) \ .$$

A similar upscaling approximation can be constructed for this system. It includes one additional numerical Greens function per coarse element corresponding to the coarse degree of freedom for p_H, i.e., for the pressure basis function w_c. Of course the final system is now nonsymmetric.

We remark that since this is an iterative technique, one could save some computation by using the pseudo-Newton method that makes use of the numerical Greens functions from a previous iterate.

6. Application to Two-Phase Immiscible, Incompressible Flow

The derivation of the governing equations of two-phase immiscible, incompressible flow is given in many references (such as [23, 13, 20]). Two differential equations (and the capillary pressure relation) result. The equations express conservation of the wetting and nonwetting fluid components, each of which is constrained to a single phase; thus, the saturation s_j is also the volumetric concentration of the jth species.

The sum of the two phase conservation equations results in a nearly second order elliptic *pressure equation.* For this equation, we use the standard global pressure formulation of Chavent [13]. When the fluids are incompressible, as we assume, the global pressure form gives a somewhat simpler equation, as it reduces the apparent coupling between the two equations.

The second equation, the *saturation equation,* is the one expressing conservation of the wetting phase. We simplify its mathematical structure by using a Kirchhoff transformation [2, 7] of the diffusive terms. The saturation equation is nearly first order hyperbolic.

Let us fix notation. We let k denote the absolute permeability of the porous medium, ϕ the porosity, and $\mathbf{g}$ the gravitational constant vector. One of our two immiscible fluids contacts the solid surfaces of the porous medium and is called the wetting phase (w), and the other is the nonwetting phase (n). Denote by $s = s_w$ the wetting and $s_n = 1-s$ the nonwetting phase saturations. Actually, we define these as the *reduced* saturations, which are linearly rescaled so that the residual saturations vanish. That is, our saturations lie between 0 (its residual value) and 1 (for which the other saturation is at its residual value).

For phase $j = w, n$, let ρ_j be the constant phase density, p_j the pressure, $\mathbf{u}_j$ the Darcy velocity, $\lambda_j(s)$ the relative mobility equal to the phase relative permeability divided by the phase viscosity, and $\lambda(s) = \lambda_w(s) + \lambda_n(s)$. The macroscopic capillary pressure $P_c(s) = p_n - p_w$ is assumed as usual to be given as a function of the saturation. The source and sinks, i.e., wells, are described by the functions q_j, $j = w, n$.

Often the medium is assumed to be incompressible, so ϕ is constant. If not, one usually assumes slight compressibility, so

$$\phi(p_w) = \phi_0 + c_r (p_w - p_0) \ , \tag{43}$$

Todd Arbogast

for some constants ϕ_0, $c_r > 0$, and p_0.

6.1. THE PRESSURE EQUATION

Let p denote the *global pressure,* a saturation dependent intermediate
pressure between the phase pressures defined as

$$p = p_n + \int_s^1 \left(\frac{\lambda_w}{\lambda} P_c' \right) (\sigma) \, d\sigma = p_w - \int_s^1 \left(\frac{\lambda_n}{\lambda} P_c' \right) (\sigma) \, d\sigma \ , \qquad (44)$$

and let $\mathbf{u} = \mathbf{u}_w + \mathbf{u}_n$ denote the total velocity. The pressure equation
is the sum of the two phase conservation equations, and it expresses
conservation of total mass. It takes the form

$$\frac{\partial \phi(p_w)}{\partial t} + \nabla \cdot \mathbf{u} = q \ , \qquad (45)$$

$$\mathbf{u} = -k\lambda(s)[\nabla p - \rho(s)\mathbf{g}] \ , \qquad (46)$$

where $q = q_w + q_n$ and

$$\rho(s) = \frac{\lambda_w(s)}{\lambda(s)} \rho_w + \frac{\lambda_n(s)}{\lambda(s)} \rho_n \ .$$

If the medium is incompressible, the time derivative of ϕ vanishes
in (45), and the equation is elliptic. Otherwise it is parabolic.

6.2. THE SATURATION EQUATION

The saturation equation expresses conservation of the wetting fluid,
written in terms of the total velocity $\mathbf{u}$ and p defined above. It is

$$\frac{\partial(\phi(p_w)s)}{\partial t} + \nabla \cdot (\psi + \gamma(s)) = q_w(s) \ , \qquad (47)$$

$$\psi = -k\nabla Q(s) \ , \qquad (48)$$

where

$$\gamma(s) = \frac{\lambda_w(s)}{\lambda(s)} \mathbf{u} - k \frac{\lambda_w(s)\lambda_n(s)}{\lambda(s)} (\rho_n - \rho_w)\mathbf{g} \ , \qquad (49)$$

$$Q(s) = -\int_0^s \frac{\lambda_w(\sigma)\lambda_n(\sigma)}{\lambda(\sigma)} p_c'(\sigma) \, d\sigma \ . \qquad (50)$$

Here, $\gamma(s)$ is the convective flux, ψ is the diffusive flux, and $Q(s)$ is the
Kirchhoff transformation that relates saturation gradients to ψ.

6.3. WELL MODELS

6.3.1. *Fixed rate wells*

Perhaps the simplest well model is to impose a fixed rate of total fluid injection $q > 0$ or extraction $q < 0$. For injection, we can independently specify $q_w > 0$ and $q_n > 0$. For extraction, we can only specify the total rate q. It is often assumed that the flow separates into phases according to the relative mobilities; that is, when $q < 0$,

$$q_j(s) = \frac{\lambda_j(s)}{\lambda(s)}q, \quad j = w, n \ . \tag{51}$$

6.3.2. *The Peaceman bottom-hole pressure well model*

Especially in the petroleum industry, it is common to adjust the pressure of the well at some fixed location, such as its bottom. The flow rate is then unknown and determined by an additional system of equations modeling the well.

For a given well, we define a well phase pressure $p_{\text{well},j}$ and a coefficient κ_j, $j = w, n$. Then the well rate is given by

$$q_j = -\kappa_j(p_j - p_{\text{well},j}) \ . \tag{52}$$

For a vertical well, we specify $p_{\text{bhp},j}$ at depth x_{bhp}, and then

$$p_{\text{well},j} = p_{\text{bhp},j} + \rho_{\text{well}}|\mathbf{g}|(x_{\text{depth}} - x_{\text{bhp}}) \ , \tag{53}$$

where x_{depth} is the depth and ρ_{well} is the average fluid density in the well, assumed to be partitioned according to the flow rate as

$$\rho_{\text{well}} = \frac{\sum_j \int \rho_j q_j}{\sum_j \int q_j} \ , \tag{54}$$

where we integrate over depth. Thus, $q_j = q_j(p_j, \rho_{\text{well}})$ and we add the latter equation to our system. Peaceman gives a formula for κ_j [24, 25] relating the grid block size and permeability to the well bore radius.

6.4. DISCRETIZATION AND SUBGRID UPSCALING

We solve the system sequentially in time. In this technique, one first solves the pressure equation, and then solves the saturation equation using the previous pressure solution (possibly extrapolated in time). After discretization of the time derivative using a backward time difference, and linearizing the equations as in a Newton procedure, both equations take the form of (1)–(2). Since this is a well-established process, we omit most of the details.

Unless bottom-hole pressure wells are used, the pressure equation is linear in p and $\mathbf{u}$. If the porous medium is incompressible, $a = 0$ in most of the domain, being nonzero only in the vicinity of wells. Thus, the algorithm of Subsection 5.4.1 is applied. Otherwise, the compressibility of the porous medium means that $a > 0$, so the algorithm of Subsection 5.4.2 can be used instead. For flexibility between the two cases, the former algorithm was chosen in our code.

The time derivative term of the saturation equation enforces $a > 0$ everywhere, so the algorithm of Subsection 5.4.2 can be used. However, generally convection dominates diffusion and dispersion, so the equation is nearly hyperbolic. It is therefore of marginal value to use the upscaling technique on the saturation equation, which applies only to the diffusion and dispersion part of the operator. Moreover, since we use a higher order method, the maximum principle is violated; that is, s can fail to lie in $[0, 1]$, which can lead to unphysical flows and/or mass balance errors. We thus solve the saturation equation on the fine grid and upscale only the pressure equation. We stress that the time consuming part of the computation is the solution of the pressure equation, so this choice is not computationally costly; upscaling the saturation equation saves little time in most applications, but upscaling the pressure equation is of great value.

7. Numerical Examples

We simulate in this section three of the more difficult phenomena to model accurately on coarse grids: near-well behavior, permeability barriers, and high permeability streaks or fractures.

7.1. SIMULATION OF WELLS

We simplify the analysis of wells by restricting to a single phase, and compute pressures near the well-bore. It is well known in the petroleum literature that the Peaceman model gives accurate simulation of pressure fields near the well bore on relatively coarse grids that do not resolve the well-bore, at least when the rock properties near the well are nearly homogeneous. In this section we consider simulation of wells using the Peaceman model, and compare and contrast simulations with grids that fully resolve the well-bore and coarser grids.

Our model two-dimensional domain is a 200m square horizontal domain with a standard 5 spot well pattern of 4 equal injectors at the corners and a bottom-hole Peaceman production well at the center. The injection rate is $0.002\text{m}^2/\text{day}$ per well, and the production well has a

radius of 0.09999m, just shy of 0.1m. The medium is incompressible, so
the porosity does not affect the equations, and homogeneous Neumann
boundary conditions are imposed.

The grids are graded in each coordinate direction, so that the wells
are better resolved than the rest of the domain. We use a simple grading
in each direction: for n points we fix $\xi_0 = 0$, ξ_1, and $\xi_n = 50$, and then
compute $\xi_i = c^{i-1}\xi_1$, where $c = (50/\xi_1)^{1/n}$, for $i = 2, 3, ..., n - 1$. This
gives a quarter of the grid, which is then reflected twice so as to cover
the domain.

7.1.1. *Simulation of wells in a homogeneous permeability field*

In this subsection we consider upscaling of the well position only, so
we take a homogeneous permeability field. In this case, the Peaceman
model is known to work well. To obtain perfect symmetry at the pro-
duction well, we simulate the full 5 spot pattern, but display only the
upper right quarter of it. In Fig. 2 (left), we see pressure contours with
a fine grid of size 199×199 with $\xi_1 = 0.1$, so the 0.2m square well-bore
is fully resolved. Upscaling to 40×40 and 20×20 coarse grids shows
excellent matches. The 10×10 grid begins to show a bit of degradation
in the quality of the match with the fine scale solution, but in this case
the coarse grid cells are approximately 20×20, so the upscaling factor
is about 400.
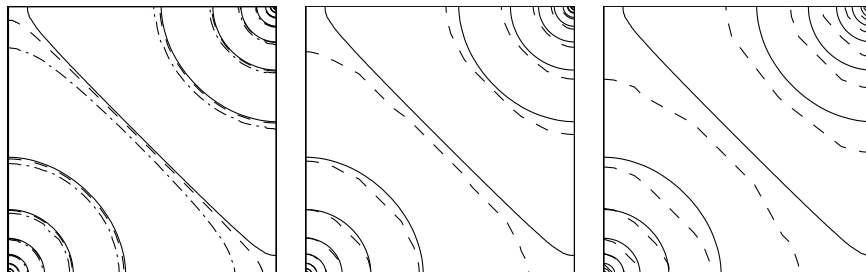
Figure 2. Pressure contours on a quarter of the domain. Left: The graded 199×199
mesh with the well-bores fully resolved. The solid lines are the fine scale solution.
The dashed lines are upscaled to 40×40, the dashed-dot lines to 20×20, and the
dotted lines to 10×10. Center: A graded 27×27 mesh, with the well grid cell 2m
square. The dashed lines are the fine scale solution, and the dotted lines are upscaled
to 3×3. Right: A graded 15×15 mesh, with the well grid cell 4m square. The dashed
lines are the fine scale solution, and the dotted lines are upscaled to 3×3. In all
figures, the solid lines are the 199×199 fully resolved fine scale solution.

In Fig. 2 (center), we consider a 27×27 mesh that does not fully
resolve the well-bores. The grid cell containing the bottom-hole pressure
well is 2m square. The fine scale solution displays the efficacy of the
Peaceman model, as the match with the fully resolved 199×199 solution
is excellent, considering that we went from 39,601 elements to 729, a

coarsening factor of about 54. A fine scale 3×3 simulation, not shown, fails miserably to resolve the pressure field, as we would expect for a coarsening factor of 4,400. However, when we *upscale* from the 27×27 grid to a 3×3 coarse grid of a mere 9 elements, we see that accuracy is maintained. The Peaceman model accounts for the grid not resolving the well-bore, and the upscaling accounts for the excessively coarse grid. As a comparison, one could fully resolve the well-bore and obtain a similar quality of solution merely by upscaling the 199×199 grid to 20×20. That is, the Peaceman well model and the upscaling technique are comparable in their ability to resolve well-bores on coarse grids with homogeneous permeability fields. Similar results are seen for a 15×15 grid in Fig. 2 (right).

7.1.2. *Simulation of wells in a heterogeneous permeability field*

While the Peaceman well model works well provided the permeability field is nearly homogeneous near the well-bore, one might expect the upscaling technique to perform well in the heterogeneous permeability case; that is the subject of our next example. We consider a five spot well pattern as in the homogeneous case, but impose a log normally distributed, but mildly correlated, permeability field as shown in Fig. 3A. The permeability varies over 3 orders of magnitude on a uniform 100×100 mesh covering the 200m square domain.

In Figs. 3B–D, we see the 100×100 fine scale pressure contours and the result of upscaling to 20×20 and 10×10 grids. Unlike the homogeneous case, there is no symmetry in this problem, so the full five spot pattern is shown, with the Peaceman well at the center. The 20×20 upscaling matches the fine scale solution relatively well, but the coarsening factor is only 25. For the 10×10 upscaling, coarsening factor 100, the match is reasonable, but noticeably different. To improve the match, we graded the coarse grid in each coordinate direction by using a distribution of 3, 9, 26, 9, 3, 3, 9, 26, 9, and 3 fine elements in each coarse block. The result is shown in Fig. 3E.

To compare these results with the Peaceman model alone, we took a 10×10 grid. The question then arises as to what averaging technique should be used on the permeability field. For our first attempt, we used on each coarse $n_x \times n_y = 10 \times 10$ block the $1/2$ power averaging rule [29], in which

$$\bar{k} = \left(\frac{1}{n_x n_y} \sum_{i,j} k_{i,j}^{1/2} \right)^2 .$$

The results showed a pressure field similar to that in Fig. 3F, but with pressures approximately 6 times too low. We then tried the composite harmonic-arithmetic averaging rule, which results in a diagonal but
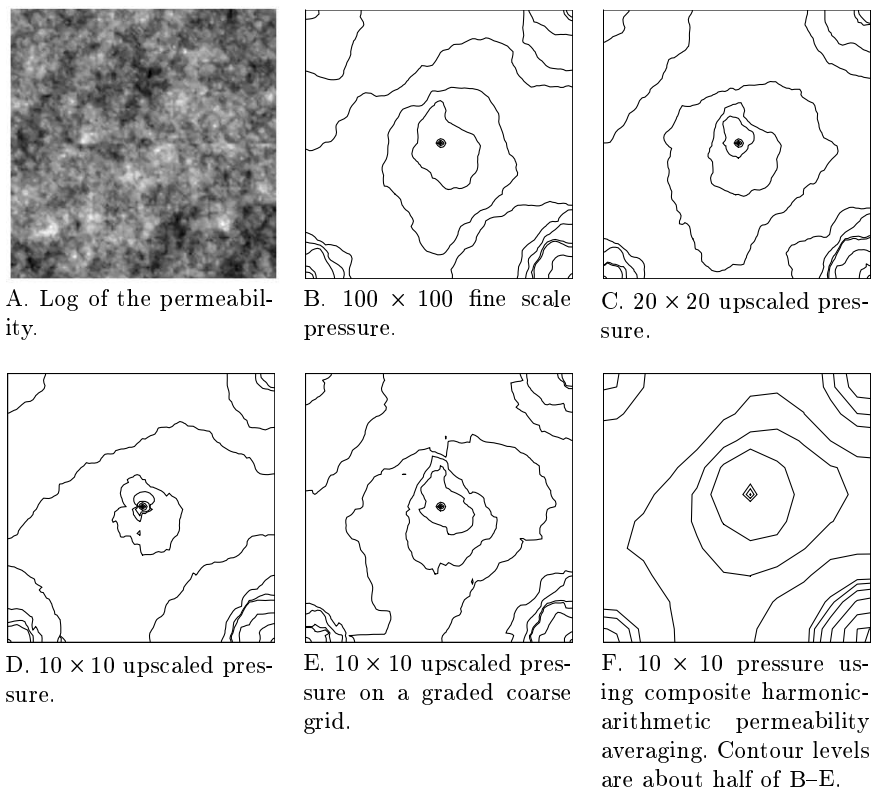
A. Log of the permeability.

B. 100 × 100 fine scale pressure.

C. 20 × 20 upscaled pressure.

D. 10 × 10 upscaled pressure.

E. 10 × 10 upscaled pressure on a graded coarse grid.

F. 10 × 10 pressure using composite harmonic-arithmetic permeability averaging. Contour levels are about half of B–E.

Figure 3. The five-spot heterogeneous well example.

nonscalar permeability. We use harmonic averaging in the flow direction and arithmetic averaging in the transverse direction. For example,

$$\bar{k}_x = \frac{1}{n_y} \sum_j \left(\frac{1}{n_x} \sum_i \frac{1}{k_{i,j}} \right)^{-1} .$$

Fig. 3F shows the pressure contours, except that the scale of pressure values has been changed to about half that in the previous four figures. This indicates that we do not have the correct average value, and leads us to our original problem of upscaling the permeability! However, even if we had found the correct average permeability, it is clear that the well is incorrectly located on the coarse grid.

7.2. Simulation of a broken pipe near a shale barrier

We return now to the two-phase problem. We remind the reader that our upscaling method is applied only to the pressure equation; the saturation equation is always solved on the fine grid. The saturation distribution is always well resolved, but since its governing equation

depends on the total velocity, we see the effect of upscaling indirectly in the saturation.

In this subsection we consider a DNAPL spill scenario. The domain is a two-dimensional vertical region of size 6m square, with a natural permeability field taken from outcrop measurements of Lawyer Canyon in Texas. The permeability data is anisotropic on a 30×30 uniform mesh, and depicted in Fig. 4. We have modified the data by placing a horizontal permeability barrier near the center of the domain of permeability 6×10^{-10}md. Otherwise the permeability varies from 3.6×10^{-2}md to 1.5×10^4md. The porosity is assumed to be constant at 0.25, and the rock and fluids are incompressible.

Horizontal component.   Vertical component.
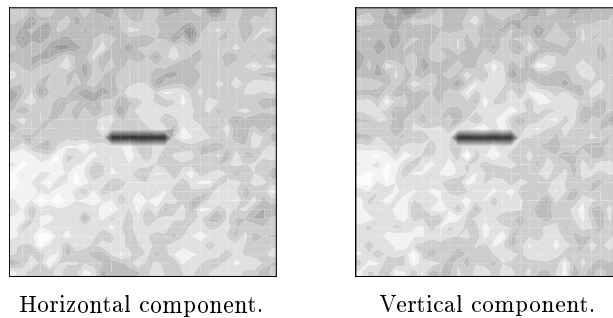
Figure 4. Log of permeability for a cross-section of Lawyer Canyon. High permeability is lighter in color.

The DNAPL is 20% more dense than water and 4 times more viscous. As if to simulate a broken underground pipe, DNAPL is injected just above and to the left of the permeability barrier at a leak rate of 6m^2/yr. A background flow of water from left to right is assumed, of speed 4m/yr on the left and 5m/yr on the right side, with no flow on the top and bottom. These are not quite physically appropriate boundary conditions, as the DNAPL cannot exit the domain. Thus the physical relevance of the simulation breaks down as DNAPL contacts the boundary.

As shown in Fig. 5, the DNAPL diffuses due to a high level of capillary pressure, and tends to the right and downward with time. Moreover, it must clearly go around the permeability barrier. We see good agreement with the simulations with upscaled global pressure to 5×5 and even 3×3 coarse meshes in Figs. 6–7. An analysis of the total velocity in Fig. 8 reveals why the match is so good: the upscaled velocity is very well resolved on the 30×30 grid, even though the pressure equation is solved on a very coarse mesh.

Since the upscaled velocity is second order accurate, we might speculate that the upscaling is not the deciding factor in the quality of the
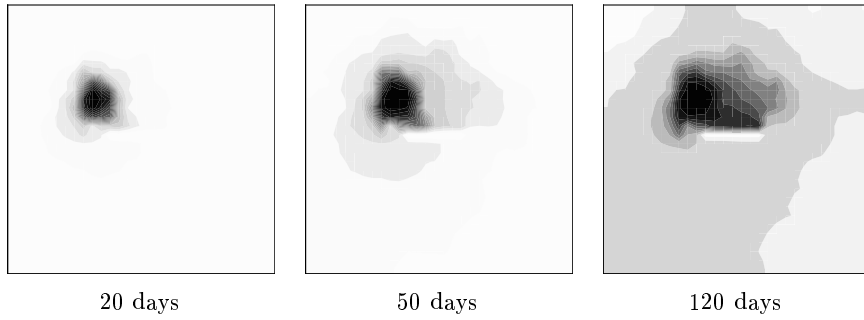
20 days   50 days   120 days

Figure 5. DNAPL saturation contours on the fine 30×30 mesh.

20 days   50 days   120 days
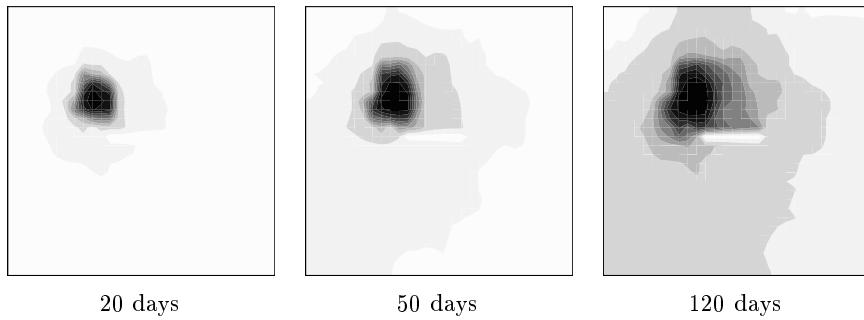
Figure 6. DNAPL saturation contours with global pressure upscaled to a 5×5 mesh.

20 days   50 days   120 days
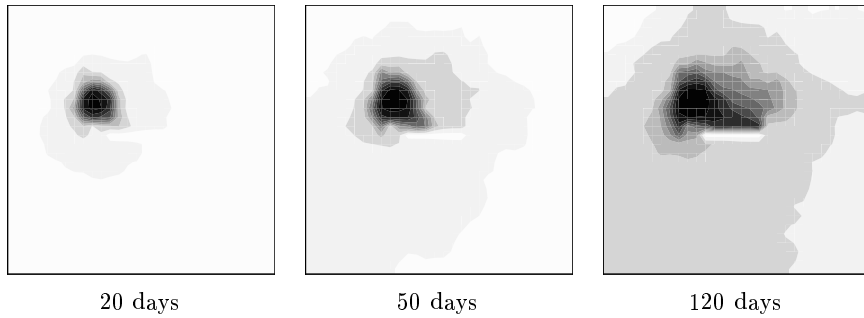
Figure 7. DNAPL saturation contours with global pressure upscaled to a 3×3 mesh.

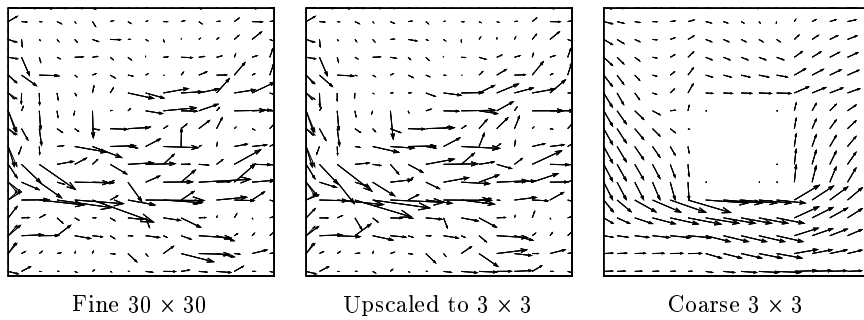Fine 30×30 Upscaled to 3×3 Coarse 3×3

Figure 8. Total velocities for the DNAPL spill scenario example.

previous results. The final diagram in Fig. 8 shows the coarse 3×3 second order accurate velocity field without using upscaling. It clearly fails to resolve the velocity, as the barrier prevents flow into the central grid element. When used to solve the 30×30 saturation equation, tremendous mass loss is observed. On each time step, the fine saturation equation injects the requisite amount of DNAPL; however, it is not transported away from the broken pipe as fast as the physics would dictate. Thus the saturation rises above 1, and is lost when it is cut off. Thus we conclude that a straightforward mixing of fine and coarse grids for the pressure and saturation equations is not appropriate near wells and spill sources. Our upscaling corrects the problem nicely, as the pressure equation is accurately approximated on the scale of the fine saturation grid.

7.3. SIMULATION OF A VERY HIGH PERMEABILITY STREAK

Perhaps the most difficult challenge is simulating flow in a fracture. We consider next a very high permeability streak, akin to a fracture, but much wider. The horizontal domain is 6m square and has a uniform 30×30 fine grid. It is oil filled, and water is injected at a rate of $0.04\text{m}^2/\text{day}$ at the lower left corner. An equal strength producer is at the upper right corner. The permeability in uniform at 100md, except for an "L"-shaped high permeability streak of magnitude $1 \times 10^{12}\text{md}$ and thickness equal to a single grid goes through the center of the domain and makes a $90°$ turn toward the injector. (The streak in clearly visible in Fig. 10.) Again the porosity is uniform at 0.25. Capillary pressure is 10 times less than in the previous broken pipe example.

From Fig. 9, we see that the pressure field is not well represented on an upscaled 5×5 mesh; however, from Fig. 10 we see that the velocity field is relatively good. The coarseness of the 5×5 mesh is visible in the upscaled velocity, but it does generally follow the high permeability streak.
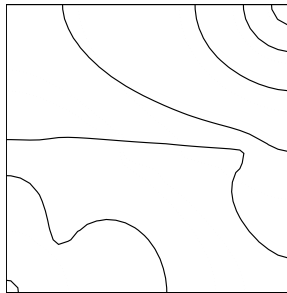
Figure 9. High permeability streak example. Contours of the pressure. The solid lines are the fine scale pressure, and the dotted lines are upscaled to 5×5.
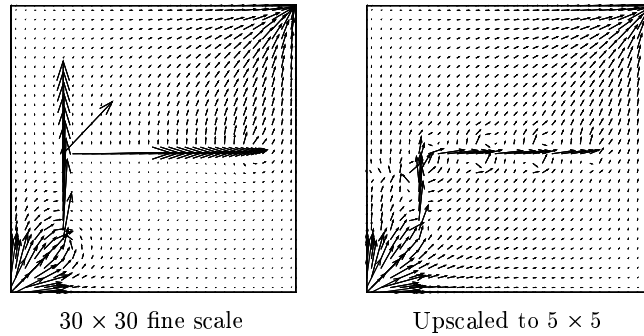
30×30 fine scale   Upscaled to 5×5

Figure 10. Total velocities at 80 days. The high permeability streak is clearly visible.

30×30 fine scale at 40 days 30×30 fine scale at 80 days

Upscaled to 5×5 at 40 days   Upscaled to 5×5 at 80 days
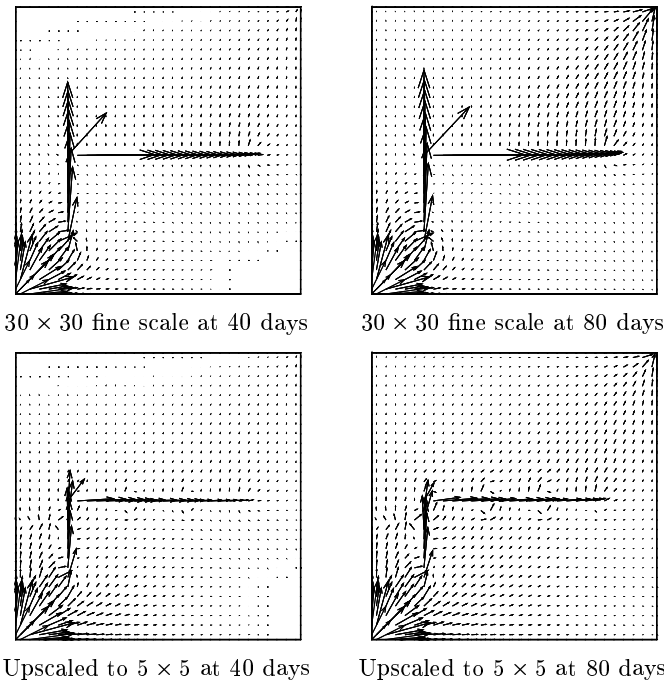
Figure 11. Water velocities at 40 and 80 days. The increase with time of the water relative permeability is easily observed.

The water velocity is also quite accurate, as depicted in Fig. 11. The nonlinear nature of the two-phase system is visible in this figure, as with time the water velocity increases downstream from the injector due to an increase in its relative permeability. This phenomena is well resolved even in the upscaled simulation.

Finally in Fig. 12 we show the fine saturation contours. The 30×30 fine solution is noticeably different from that using a total velocity upscaled to 5×5; however, considering the difficulty of the problem, the match is remarkable.

30×30 fine scale at 40 days 30×30 fine scale at 80 days

Upscaled to 5×5 at 40 days   Upscaled to 5×5 at 80 days
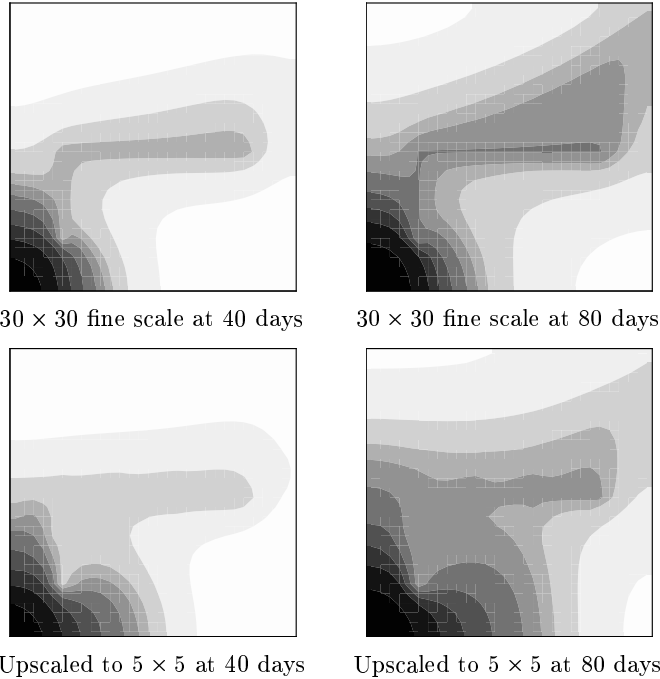
Figure 12. Water saturation at 40 and 80 days. Fluid clearly travels through the high permeability streak.

8. Conclusions

We presented a numerical subgrid upscaling approach that allows most of the computational work to be confined to an upscaled problem defined on a coarse grid. The method results in a fine scale representation of the solution that is locally conservative on the fine scale. The method involves a coarse grid scale operator coupled to a subgrid scale operator. The numerical Greens function technique allows us to solve the subgrid part of the problem independently of the coarse grid.

The method can be applied to the system of equations governing two-phase flow in a porous medium. One advantage of the method is that we use data provided on the fine scale directly. Therefore, no assumptions are made about the physics or the expected directions of flow, and no effective permeabilities or pseudo-functions result.

Our numerical examples show the performance of upscaling the pressure equation when coupled to a fully resolved saturation equation. We considered three difficult numerical examples involving near-well behavior, permeability barriers, and high permeability streaks or fractures. We found remarkably good agreement between fully resolved fine

scale solutions and solutions upscaled to very coarse grids with factors of upscaling around 100.

Acknowledgements

References

1. Amaziane, B., A. Bourgeat, and J. Koebbe: 1991, 'Numerical simulation and homogenization of two-phase flow in heterogeneous porous media'. *Transport in Porous Media* **9**, 519–547.
2. Arbogast, T.: 1992, 'The existence of weak solutions to single-porosity and simple dual-porosity models of two-phase incompressible flow'. *Journal of Nonlinear Analysis: Theory, Methods, and Applications* **19**, 1009–1031.
3. Arbogast, T.: 2000, 'Numerical subgrid upscaling of two-phase flow in porous media'. In: Z. Chen et al. (eds.): *Numerical treatment of multiphase flows in porous media*, Vol. 552 of *Lecture Notes in Physics*. Berlin: Springer, pp. 35–49.
4. Arbogast, T. and S. Bryant: 2000, 'Efficient forward modeling for DNAPL site evaluation and remediation'. In: Bentley et al. (eds.): *Computational Methods in Water Resources XIII*. Rotterdam, pp. 161–166.
5. Arbogast, T. and S. Bryant: February 11–14, 2001, 'Numerical subgrid upscaling for waterflood simulations'. In: *Proceedings of the 16th SPE Symposium on Reservoir Simulation held in Houston, Texas*. SPE 66375.
6. Arbogast, T., S. E. Minkoff, and P. T. Keenan: 1998, 'An operator-based approach to upscaling the pressure equation'. In: V. N. Burganos et al. (eds.): *Computational Methods in Water Resources XII*, Vol. 1. Southampton, U.K., pp. 405–412.
7. Arbogast, T., M. F. Wheeler, and N.-Y. Zhang: 1996, 'A nonlinear mixed finite element method for a degenerate parabolic equation arising in flow in porous media'. *SIAM J. Numer. Anal.* **33**, 1669–1687.
8. Arnold, D. N. and F. Brezzi: 1985, 'Mixed and nonconforming finite element methods: implementation, postprocessing and error estimates'. *RAIRO Modél. Math. Anal. Numér.* **19**, 7–32.
9. Brezzi, F.: 1999, 'Interacting with the subgrid world'. In: *Proceedings of the Dundee Conference*.
10. Brezzi, F., J. Douglas, Jr., R. Duràn, and M. Fortin: 1987, 'Mixed finite elements for second order elliptic problems in three variables'. *Numer. Math.* **51**, 237–250.
11. Brezzi, F., J. Douglas, Jr., and L. D. Marini: 1985, 'Two families of mixed elements for second order elliptic problems'. *Numer. Math.* **47**, 217–235.
12. Brezzi, F. and M. Fortin: 1991, *Mixed and hybrid finite element methods*. New York: Springer-Verlag.

13. Chavent, G. and J. Jaffré: 1986, *Mathematical models and finite elements for reservoir simulation*. New York: Elsevier Science Publishers.

14. Chen, Z.: 1994, 'Large-scale averaging analysis of single phase flow in fractured reservoirs'. *SIAM J. Appl. Math.* **54**, 641–659.

15. Glowinski, R. and M. F. Wheeler: 1988, 'Domain decomposition and mixed finite element methods for elliptic problems'. In: R. Glowinski et al. (eds.): *First International Symposium on Domain Decomposition Methods for Partial Differential Equations*. Philadelphia: SIAM, pp. 144–172.

16. Hornung, U. (ed.): 1997, *Homogenization and Porous Media*, Interdisciplinary Applied Mathematics Series. New York: Springer-Verlag. To appear.

17. Hou, T. Y. and X. H. Wu: 1997, 'A multiscale finite element method for elliptic problems in composite materials and porous media'. *J. Comput. Phys.* **134**, 169–189.

18. Hughes, T. J. R.: 1995, 'Multiscale phenomena: Green's functions, the Dirichlet-to-Neumann formulation, subgrid scale models, bubbles and the origins of stabilized methods'. *Comp. Meth. in Appl. Mech. and Engng.* **127**, 387–401.

19. Hughes, T. J. R., G. R. Feijóo, L. Mazzei, and J.-B. Quincy: 1998, 'The variational multiscale method—a paradigm for computational mechanics'. *Comp. Meth. in Appl. Mech. and Engng.* **166**, 3–24.

20. Lake, L. W.: 1989, *Enhanced Oil Recovery*. Englewood Cliffs, New Jersey: Prentice Hall.

21. Oden, J. T. and K. S. Vemaganti: 1999, 'Adaptive hierarchical modeling of heterogeneous structures'. *Phys. D: Nonlin. Phenomena* **133**, 404–415.

22. Oden, J. T. and K. S. Vemaganti: 2000, 'Estimation of local modeling error and goal-oriented adaptive modeling of heterogeneous materials. I. Error estimates and adaptive algorithms'. *J. Comput. Phys.* **164**, 22–47.

23. Peaceman, D. W.: 1977, *Fundamentals of numerical reservoir simulation*. Amsterdam: Elsevier.

24. Peaceman, D. W.: 1978, 'Interpretation of well-block pressures in numerical reservoir simulation'. *Society of Petroleum Engineers Journal* pp. 183–194.

25. Peaceman, D. W.: 1983, 'Interpretation of well-block pressures in numerical reservoir simulation with nonsquare grid blocks and anisotropic permeability'. *Society of Petroleum Engineers Journal* pp. 531–543.

26. Peszynska, M., M. F. Wheeler, and I. Yotov: 2001, 'Mortar upscaling for multiphase flow in porous media'. *submitted*.

27. Quintard, M. and S. Whitaker: 1988, 'Two-phase flow in heterogeneous porous media: The method of large-scale averaging'. *Transport in Porous Media* **3**, 357–413.

28. Raviart, R. A. and J. M. Thomas: 1977, 'A mixed finite element method for 2nd order elliptic problems'. In: *Mathematical Aspects of Finite Element Methods*, No. 606 in Lecture Notes in Math. New York: Springer, pp. 292–315.

29. Romeu, R. K. and B. Noetinger: 1995, 'Calculation of internodal transmissivities in finite difference models of flow in heterogeneous porous media'. *Water Resources Research* **31**, 943–959.

30. Thomas, J. M.: 1977, 'Sur l'analyse numerique des methodes d'elements finis hybrides et mixtes'. Ph.D. thesis, Sciences Mathematiques, à l'Universite Pierre et Marie Curie.

31. Xu, J.: 2001, 'The method of subspace corrections'. *J. Computational and Appl. Math.* **128**, 335–362.